

Controlling spin current polarization through non-collinear antiferromagnetism

T. Nan¹, C. X. Quintela¹, J. Irwin², G. Gurung³, D. F. Shao³, J. Gibbons⁴, N. Campbell², K. Song⁵, S. Y. Choi⁶, L. Guo¹, R. D. Johnson^{7,8,9}, P. Manuel⁹, R. V. Chopdekar¹⁰, I. Hallsteinsen^{10,11}, T. Tybell¹², P. J. Ryan^{12,13}, J. W. Kim¹², Y. S. Choi¹², P. G. Radaelli⁷, D. C. Ralph^{4,14}, E. Y. Tsymbal³, M. S. Rzechowski², C. B. Eom^{1*}

Abstract

The interconversion of charge and spin currents via spin-Hall effect is essential for spintronics. Energy-efficient and deterministic switching of magnetization can be achieved when spin polarizations of these spin currents are collinear with the magnetization. However, symmetry conditions generally restrict spin polarizations to be orthogonal to both the charge and spin flows. Spin polarizations can deviate from such direction in nonmagnetic materials only when the crystalline symmetry is reduced. Here we show control of the spin polarization direction by using a non-collinear antiferromagnet Mn_3GaN , in which the triangular spin structure creates a low magnetic symmetry while maintaining a high crystalline symmetry. We demonstrate that epitaxial Mn_3GaN /Permalloy heterostructures can generate unconventional spin-orbit torques at room temperature corresponding to out-of-plane and Dresselhaus-like spin polarizations which are forbidden in any sample with two-fold rotational symmetry. Our results demonstrate an approach based on spin-structure design for controlling spin-orbit torque, enabling high-efficient antiferromagnetic spintronics.

¹Department of Materials Science and Engineering, University of Wisconsin-Madison, Madison, Wisconsin 53706, USA;

²Department of Physics, University of Wisconsin-Madison, Madison, Wisconsin 53706, USA; ³Department of Physics and Astronomy & Nebraska Center for Materials and Nanoscience, University of Nebraska, Lincoln, NE 68588, USA; ⁴Laboratory of Atomic and Solid State Physics, Cornell University, Ithaca, New York 14853, USA; ⁵Department of Materials Modeling and Characterization, KIMS, Changwon 51508, South Korea; ⁶Department of Materials Science and Engineering, POSTECH, Pohang 37673, South Korea; ⁷Clarendon Laboratory, Department of Physics, University of Oxford, Parks Road, Oxford OX1 3PU, UK; ⁸ISIS Facility, Rutherford Appleton Laboratory, Chilton, Didcot, OX11 0QX, UK; ⁹Department of Physics and Astronomy, University College London, Gower Street, London, WC1E 6BT, UK; ¹⁰Advanced Light Source, Lawrence Berkeley National Laboratory (LBNL), 1 Cyclotron Road, Berkeley, California 94720, USA; ¹¹Department of Electronic Systems, Norwegian University of Science and Technology, Trondheim 7491, Norway; ¹²Advanced Photon Source, Argonne National Laboratory, Argonne, Illinois 60439, USA; ¹³School of Physical Sciences, Dublin City University, Dublin 11, Ireland; ¹⁴Kavli Institute at Cornell for Nanoscale Science, Ithaca, New York 14853, USA

* Corresponding author. Email: eom@engr.wisc.edu

Current-induced spin-orbit torque enables highly efficient manipulation of magnetization for spintronic applications¹⁻⁸. In the classical picture of current-induced magnetization dynamics^{9,10} (Fig. 1f), charge currents in a multilayer sample flowing along the in-plane direction (\mathbf{x} direction) can generate out-of-plane spin currents (flowing in the \mathbf{z} direction) that have spin polarization $\boldsymbol{\sigma}$, required by symmetry to be along the \mathbf{y} direction corresponding to a Rashba-like spin polarization. This particular spin current can give rise to an anti-damping spin torque in an adjacent ferromagnet, which has magnetization vector \mathbf{m} , of the form $\mathbf{m} \times (\mathbf{m} \times \mathbf{y})$. The anti-damping torque is responsible for efficient magnetization manipulation when the torque is collinear with the magnetization leading to a direct change of the effective magnetic damping. But as the anti-damping torque is restricted to lie along an in-plane direction, it is efficient for manipulating only samples with magnetic anisotropy along the in-plane \mathbf{y} axis not that along the out-of-plane (\mathbf{z} direction) or collinear with the current (\mathbf{x} direction). Such a limitation of controlling the spin-torque or spin polarizations makes the switching of magnetic devices with magnetic anisotropy along \mathbf{x} or \mathbf{z} axis nondeterministic and much less efficient (than that along \mathbf{y} direction)¹¹.

To efficiently and deterministically drive, for example, perpendicularly-magnetized devices that are preferred for high-density memories, an out-of-plane anti-damping torque is required. Such an out-of-plane spin-torque can originate from spin-orbit scattering from ferromagnetic interfaces¹²⁻¹⁴, or can arise at the interface in systems with reduced symmetry, such as in bilayers of the non-magnetic transition-metal dichalcogenide and ferromagnetic metals¹⁵. However, these effects based on interface or heterostructure engineering have not been demonstrated strong enough for practical anti-damping switching. Here we demonstrate an alternative strategy to achieve unconventional spin-orbit torques, based on long-range non-collinear magnetic order within the *bulk* of the spin-source layer. In particular, we use the spin-Hall effect in epitaxial thin films of Mn_3GaN , a metallic antiferromagnet that has a 120° triangular spin texture, which reduces the symmetry sufficiently to allow spin current generation with different spin polarization directions to generate unconventional spin-torques. In heterostructures of epitaxial Mn_3GaN /Permalloy, we observe not only the out-of-plane anti-damping torque, but also the anti-damping torque corresponding to a Dresselhaus-like spin polarization¹⁶⁻¹⁸, besides the conventional Rashba-like symmetry. When the non-collinear spin texture is eliminated by heating above the Néel temperature of Mn_3GaN (345 K), the unconventional spin-torques go to zero. Such a control of the spin polarizations is coincident with our symmetry analysis and theory calculation upon the magnetic space groups across the Néel transition. Previously, although the spin-Hall effect has been demonstrated in antiferromagnetic thin films, only Rashba-like symmetry has been observed¹⁹⁻²².

Mn_3GaN is a metallic nitride with the antiperovskite crystal structure^{23,24} (identical to the perovskite structure, but with anion and cation positions interchanged) and a lattice parameter close to that of commonly used perovskite oxide substrates. In the bulk, it is known to exhibit antiferromagnetic ordering with a non-collinear Γ^{5g} Kagome-like structure (magnetic space group: $R\bar{3}m$) stabilized by the magnetic frustration of the Mn atoms in the (111) plane (Fig. 1a)^{23,25}. In the (001) plane of Mn_3GaN (Fig. 1b), the (110) plane is the only mirror plane. In this low-symmetry state, we find that charge currents along \mathbf{x} generate unconventional anti-damping torque components in the form of $\boldsymbol{\tau}_x \propto \mathbf{m} \times (\mathbf{m} \times \mathbf{x})$ and $\boldsymbol{\tau}_z \propto \mathbf{m} \times (\mathbf{m} \times \mathbf{z})$ in addition to the conventional $\boldsymbol{\tau}_y \propto \mathbf{m} \times (\mathbf{m} \times \mathbf{y})$, which correspond to spin currents with $\boldsymbol{\sigma}$ along \mathbf{x} , \mathbf{z} and \mathbf{y} , respectively (Fig. 1c). These spin-polarized currents have corresponding spin-Hall conductivities σ_{zx}^x , σ_{zx}^z and σ_{zx}^y (in the form of σ_{jk}^i , where i, j and k denote the spin polarization, spin flow and charge flow directions). The symmetry allowed, and experimentally observed, non-zero spin-Hall conductivities are consistent with our linear theory calculation (Supplementary Note 9). Figure 1d shows that the σ_{zx}^x , σ_{zx}^z and σ_{zx}^y calculated by using the bulk Mn_3GaN band structure are large within a wide energy window around the charge neutrality point, implying the existence of a sizable spin-Hall current

even in the presence of charge carrier doping by defects. Above the antiferromagnetic-to-paramagnetic transition temperature (Néel temperature T_N), disordered spins give rise to a high-symmetry state (space group: $Pm\bar{3}m$) having 4 mirror planes in the crystal lattice (Fig. 1e), and consequently only the conventional spin-Hall conductivity σ_{zx}^y can be non-zero. We list the matrices of the spin-Hall conductivity tensors, obtained from symmetry analysis and calculations, for Mn_3GaN in antiferromagnetic and paramagnetic phases in the Supplementary Table 1.

Results

Epitaxial Mn_3GaN thin films were grown on (001) $(La_{0.3}Sr_{0.7})(Al_{0.65}Ta_{0.35})O_3$ (LSAT) substrates by reactive magnetron sputtering with *in-situ* reflection high-energy electron diffraction (RHEED, see Methods). The out-of-plane x-ray diffraction around the (002) LSAT substrate peak shows an epitaxial Mn_3GaN film (Fig. 2a). The distinct Kiessig fringes around the Mn_3GaN (002) peak (Fig. 2a) and the streaky RHEED pattern of the Mn_3GaN film surface (Fig. 2a inset) indicate a high crystalline quality and a smooth film surface. We also confirmed the cube-on-cube epitaxial relationship between the Mn_3GaN film and underlying LSAT substrate (Supplementary Note 1). Ferromagnetic permalloy $Ni_{81}Fe_{19}$ (Py) and the Cu (as a spacer layer) thin films were then deposited *in situ* on Mn_3GaN to form the Py/Cu/ Mn_3GaN bilayer, and finally were patterned into device bars for spin-torque measurements. In Fig. 2b, we show the cross-sectional filtered STEM-HAADF image of the bilayer, which reveals sharp interfaces between both Mn_3GaN /LSAT (left) and Py/ Mn_3GaN (right). Atomic force microscope images of the 10 nm Py/20 nm Mn_3GaN surface indicate an atomically-smooth surface with a surface roughness of ~ 0.3 nm. Using neutron diffraction, we determined that our 200-nm Mn_3GaN films order with the bulk antiferromagnetic triangular Γ^{5g} spin structure below a Néel temperature of $T_N=350$ K (Supplementary Note 3), slightly higher than for the thinner 20-nm films having $T_N=345$ K, and higher than that for polycrystalline bulk samples ($T_N\sim 290$ K), possibly due to less grain boundaries and slight nitrogen deficiency in thin film samples (Supplementary Note 2). Using x-ray magnetic linear and circular dichroism with photoemission electron microscopy, we observe antiferromagnetic domains with size on the order of 200-300 nm (Supplementary Note 12). We note that domains with differing spin configurations can affect the unconventional spin torque, since the unconventional spin-Hall conductivity terms can be averaged out to zero under certain symmetry operations (Supplementary Note 11). The fact that we observe non-zero unconventional spin torques in Mn_3GaN , as described below, suggests that certain antiferromagnetic domain configurations are more favorable, which is inferred to be due to a tetragonal distortion that can induce a small non-compensated magnetic moment in Mn_3GaN thin films. This unbalanced antiferromagnetic domain population is also evidenced by the finite x-ray magnetic linear dichroism (XMLD) signal from the Mn_3GaN films at the Mn edge for a beam area 100's of microns in scale (Supplementary Note 12).

To measure the symmetry of the spin torques, we use the spin-torque ferromagnetic resonance (ST-FMR) technique (Fig. 3a)^{15,26}. During the ST-FMR measurement, a microwave current applied to Mn_3GaN produces alternating torques on the Py, and excites the Py magnetic moment into precession, generating a corresponding alternating sinusoidal change of the resistance R due to the anisotropic magnetoresistance (AMR) of Py. We measure a dc voltage signal V_{mix} across the device bar that arises from the mixing between the alternating current and changes in the device resistance. The resonance in V_{mix} is obtained by sweeping the external in-plane magnetic field through the Py resonance condition (see Methods). Both in-plane and out-of-plane torque components can then be determined individually, as the symmetric and antisymmetric part of the line shape are proportional to the amplitude of the in-plane and out-of-plane torque components, respectively. Considering only the conventional spin-Hall effect (or the Rashba-Edelstein effect and Oersted field), the in-plane and out-of-plane torque components would only have the form of $\mathbf{m} \times (\mathbf{m} \times \mathbf{y})$ and $\mathbf{m} \times \mathbf{y}$, respectively^{8,27}. This corresponds to the case of samples containing materials with 2-fold rotational

symmetry, in which case if \mathbf{m} is inverted by rotating the in-plane magnetic field angle φ (with respect to \mathbf{x}) by 180° , V_{mix} must retain the same amplitude but change sign, giving $V_{\text{mix}}(\varphi) = -V_{\text{mix}}(\varphi + 180^\circ)$. Any difference in the resonance line shape between $V_{\text{mix}}(\varphi)$ and $-V_{\text{mix}}(\varphi + 180^\circ)$ indicates the presence of an additional, unconventional torque component.

Fig. 3b shows resonance spectra of the 10 nm Py/2 nm Cu/20 nm Mn_3GaN sample with the current flow along the $[100]$ direction for the magnetic field angle φ equal to 40° and 220° , measured at room temperature when the Mn_3GaN is in the antiferromagnetic state. The Cu insertion layer breaks the exchange coupling at the Py/ Mn_3GaN interface, but it allows the transmission of the spin current since Cu has a long spin diffusion length. We find that the $V_{\text{mix}}(40^\circ)$ and $-V_{\text{mix}}(220^\circ)$ scans are notably different in the antiferromagnetic phase, indicating the presence of unconventional torque components¹⁵.

To examine the torque components quantitatively, we perform ST-FMR measurements as a function of the in-plane magnetic field angle φ . Fig. 3c and d shows the angular dependence of symmetric V_S and antisymmetric V_A part for the 10 nm Py/2 nm Cu/20 nm Mn_3GaN sample, measured at room temperature. The angular dependence of ST-FMR can be understood as the product of the AMR in Py [$dR/d\varphi \propto \sin(2\varphi)$], with the in-plane τ_{\parallel} or out-of-plane torque τ_{\perp} components, as $V_S \propto \sin(2\varphi)\tau_{\parallel}$ and $V_A \propto \sin(2\varphi)\tau_{\perp}$. For ferromagnetic metal/normal metal bilayers (i.e. Py/Pt), the conventional anti-damping torque $\boldsymbol{\tau}_{\text{y,AD}} \propto \mathbf{m} \times (\mathbf{m} \times \mathbf{y})$ and field-like torque $\boldsymbol{\tau}_{\text{y,FL}} \propto \mathbf{m} \times \mathbf{y}$ both have a $\cos(\varphi)$ dependence, giving rise to an overall angular dependence of the form $\sin(2\varphi)\cos(\varphi)$ for both V_S and V_A . We find the angular dependence of both V_S and V_A for the Mn_3GaN clearly deviate from this simple model (Fig. 3c and d, grey line), but can be well fitted by adding additional, unconventional torque terms with the presence of spin currents with spin polarizations oriented away from \mathbf{y} . The spin currents that are polarized along \mathbf{x} would generate torque [$\boldsymbol{\tau}_{\text{x,AD}} \propto \mathbf{m} \times (\mathbf{m} \times \mathbf{x})$ and $\boldsymbol{\tau}_{\text{x,FL}} \propto \mathbf{m} \times \mathbf{x}$] with a $\sin(\varphi)$ dependence; while the torques with spin polarization along \mathbf{z} [$\boldsymbol{\tau}_{\text{z,AD}} \propto \mathbf{m} \times (\mathbf{m} \times \mathbf{z})$ and $\boldsymbol{\tau}_{\text{z,FL}} \propto \mathbf{m} \times \mathbf{z}$], since \mathbf{m} is oriented in the plane, are independent of φ . We thus fit $V_{\text{mix},S}(\varphi)$ and $V_{\text{mix},A}(\varphi)$ to more general forms to take all possible torque terms into account:

$$V_{\text{mix},S}(\varphi) = \sin(2\varphi) (\tau_{\text{x,AD}} \sin(\varphi) + \tau_{\text{y,AD}} \cos(\varphi) + \tau_{\text{z,FL}}) \quad (1)$$

$$V_{\text{mix},A}(\varphi) = \sin(2\varphi) (\tau_{\text{x,FL}} \sin(\varphi) + \tau_{\text{y,FL}} \cos(\varphi) + \tau_{\text{z,AD}}) \quad (2)$$

From the fitting, we find non-zero anti-damping torque terms $\tau_{\text{x,AD}}$, $\tau_{\text{y,AD}}$ and $\tau_{\text{z,AD}}$ demonstrating the existence of unconventional torque originated from spin polarizations along \mathbf{x} and \mathbf{z} . This is consistent with the symmetry-allowed spin currents derived from the non-collinear antiferromagnetic Mn_3GaN magnetic space group through the bulk spin-Hall effect. This mechanism is distinct from those previously reported in noncentrosymmetric systems, and in magnetic tri-layers^{13,14}. The generation of the spin torque $\boldsymbol{\tau}_{\text{v,AD}}$ relative to the charge current density can be parameterized into the spin-torque ratio $\theta_v = \frac{\hbar}{2e} \frac{j_{s,v}}{j_c}$, where $j_{s,v}$ is the spin current density with the spin polarization along \mathbf{v} that is absorbed by the Py, and j_c is the charge current density in Mn_3GaN estimated from a parallel-conduction model. We find at room temperature that $\theta_x = -0.013 \pm 0.0002$, $\theta_y = 0.025 \pm 0.0002$ and $\theta_z = 0.019 \pm 0.0005$, and the spin torque conductivity ($\sigma_{zx}^v = \frac{\theta_v}{\rho} \frac{\hbar}{2e}$, where ρ is the charge resistivity of Mn_3GaN) to be around $\sigma_{zx}^x = -5.9 \times 10^3 (\hbar/2e)(\Omega \text{ m})^{-1}$, $\sigma_{zx}^y = 1.1 \times 10^4 (\hbar/2e)(\Omega \text{ m})^{-1}$ and $\sigma_{zx}^z = 8.6 \times 10^3 (\hbar/2e)(\Omega \text{ m})^{-1}$ with $\rho = 220 \mu\Omega \text{ cm}$. The out-of-plane field-like torque has the form $\boldsymbol{\tau}_{\text{y,FL}}$, dominated by the contribution from the current-induced Oersted field (see Methods) with no detectable $\boldsymbol{\tau}_{\text{x,FL}}$ torque. In addition, we observe an in-plane field-like torque $\boldsymbol{\tau}_{\text{z,FL}}$ with a large torque ratio of $\theta_{\text{FL},z} = -0.15 \pm 0.0002$, which

could be generated along with $\tau_{z,AD}$ by the spin currents polarized along \mathbf{z} . The observed unconventional spin torques could also originate from spin-orbit procession,¹³ in which a longitudinal spin polarized current from a ferromagnet can scatter from the ferromagnetic/normal metal interface. We note that the longitudinal spin polarized current in the non-collinear antiferromagnet and the transverse spin current that is reported in this paper could share the same physical origin²⁸.

We further confirmed the correlation between the observed unconventional spin polarization and the non-collinear spin structures in Mn_3GaN by performing angular-dependent ST-FMR measurements across its antiferromagnetic-to-paramagnetic phase transition. The Néel temperature of the 20 nm Mn_3GaN thin film is determined to be 345 K by tracking the temperature dependence of the out-of-plane lattice parameter (Fig. 4a) because the magnetic phase transition of Mn_3GaN produces a region of strong negative thermal expansion²⁹. Fig. 4b-d show the temperature dependence (300 K to 380 K) of the ratios between anti-damping torque components and the Oersted torque, $\tau_{y,AD}/\tau_{y,FL}$, $\tau_{x,AD}/\tau_{y,FL}$ and $\tau_{z,AD}/\tau_{y,FL}$ (extracted from the full angular dependent ST-FMR measured at each temperature, see Supplementary Note 7). The unconventional torque ratios $\tau_{x,AD}/\tau_{y,FL}$ and $\tau_{z,AD}/\tau_{y,FL}$ vanish when the sample temperature is above the Néel temperature, while the conventional component $\tau_{y,AD}/\tau_{y,FL}$ remains non-zero, with a weak peak near the transition temperature (a similar peak in $\tau_{y,AD}$ has been observed near the Curie temperature of $\text{Fe}_x\text{Pt}_{1-x}$ alloys³⁰). The vanishing of $\tau_{x,AD}/\tau_{y,FL}$ and $\tau_{z,AD}/\tau_{y,FL}$ directly demonstrates the strong correlation between the non-collinear spin structure and the existence of the unconventional spin torques. We also find that the unconventional torques persist at temperatures well below the Néel temperature (Supplementary Note 8), but decrease gradually at lower temperature with the increase of the uncompensated moment and the onset of the anomalous Hall effect in Mn_3GaN (Supplementary Note 4 and 5). The correlation between the observed unconventional spin-orbit torques, the canted moment and the anomalous Hall effect in Mn_3GaN at low temperatures requires further study.

Discussion

In summary, we have demonstrated the generation of unconventional spin-orbit torque based on low-symmetry non-collinear spin ordering present in the bulk of an epitaxial antiferromagnetic thin film with an antiperovskite structure. Such unconventional torques can be robustly manipulated by controlling the antiferromagnetic ordering across the Néel temperature. This work provides essential insight into understanding how unconventional spin-orbit torques can arise in systems with lower crystalline or magnetic symmetry. This strategy of controlling the spin polarization direction by the design of the spin structure will lead to a much more efficient manipulation and deterministic switching of nano-magnets with arbitrary magnetization, as well as antiferromagnetic tunnel junctions²⁸. In addition, our finding offers the possibility to design and control spin currents through manipulating the non-collinear spin order via strain, temperature, chemical doping, and possibly external excitation, opening new areas of research opportunities in antiferromagnetic spintronics^{31–35}.

Methods

Sample growth, fabrication and characterization

Epitaxial Mn_3GaN thin films were grown on (001)-oriented LSAT substrates by DC reactive magnetron sputtering using a stoichiometric Mn_3Ga target in a vacuum chamber with a base pressure of 1×10^{-8} Torr. During the growth, the Mn_3GaN growth mode and surface crystalline structure were monitored by *in situ* reflection high energy electron diffraction (RHEED). The growth undergoes a 3D to 2D growth mode transition. The streaky RHEED pattern after the deposition implies a smooth film surface (Fig. 2a inset).

The growth was performed at a substrate temperature of 550 °C and an Ar (62 sccm)/N₂ (8 sccm) atmosphere of 10 mTorr. After the Mn₃GaN growth, the sample was cooled down in vacuum. The Cu and Py thin films were subsequently sputter deposited at an Ar pressure of 3 mTorr. The atomically flat sample surface was verified using atomic force microscopy (Supplementary Figure 1). We confirmed the thickness, epitaxial arrangement, and coherence of the Mn₃GaN films using x-ray reflectivity, x-ray diffraction, and reciprocal space mappings. The growth rate of Py and Cu films were calibrated using x-ray reflectivity.

We patterned the samples by using photolithography followed by ion beam milling. Then 200 nm Pt/5 nm Ti electrodes were sputter deposited and defined by a lift-off procedure. Devices for ST-FMR were patterned into microstrips (20-50 μm wide and 40-100 μm long) with ground-signal-ground electrodes. Devices for electrical transport measurements were patterned into 100 μm wide and 500 μm long Hall bars.

STEM measurements

The STEM sample was prepared through mechanical polishing down to a thickness of ~10 μm by using the precise polishing system (EM TXP, Leica). The polished specimen was then ion-milled using a 1-3 keV Ar ion beam (PIPS II, Gatan) to make the hole for the STEM observation. Afterwards, a low energy milling was performed using 0.1 keV Ar beam to minimize the surface damage from the prior ion-milling process.

The atomic structures were observed using a STEM (JEM-ARM200F, JEOL) at 200 kV equipped with an aberration corrector (ASCOR, CEOS GmbH). The optimum size of the electron probe was ~0.8 Å. The collection semi-angles of the HAADF detector were adjusted from 68 to 280 mrad in order to collect large-angle elastic scattering electrons for clear Z-sensitive images. The obtained raw images were processed with a band-pass Wiener filter with a local window to reduce a background noise (HREM research Inc.).

ST-FMR measurements

During ST-FMR measurements, a microwave current at a fixed frequency was applied with the in-plane magnetic field swept from 0-0.2 T for driving the ferromagnetic layer Py through its resonance condition. The amplitude of the microwave current is modulated at a low frequency (1.713 kHz), and the mixing voltage is detected through a lock-in amplifier. For the low temperature ST-FMR measurements (including the room temperature results shown in Fig. 3), the device was wire bonded to a coplanar waveguide and then transferred into a liquid helium flow cryostat. For the high temperature measurements (Fig. 4), the sample is placed on a resistive heater with the device probed by the ground-signal-ground rf probe. The ST-FMR resonance line shape can be fitted to a sum of symmetric V_S and antisymmetric V_A Lorentzian components in the form $V_{\text{mix}} = V_{\text{mix},S} \frac{W^2}{(\mu_0 H_{\text{ext}} - \mu_0 H_{\text{FMR}})^2 + W^2} + V_{\text{mix},A} \frac{W(\mu_0 H_{\text{ext}} - \mu_0 H_{\text{FMR}})}{(\mu_0 H_{\text{ext}} - \mu_0 H_{\text{FMR}})^2 + W^2}$, where W is the half-width-at-half-maximum resonance linewidth, μ_0 is the permeability in vacuum and H_{FMR} is the resonance field. The in-plane τ_{\parallel} and out-of-plane τ_{\perp} components are proportional to $V_{\text{mix},S}$ and $V_{\text{mix},A}$ components, which can be expressed as,

$$V_{\text{mix},S} = -\frac{I_{\text{rf}}}{2} \left(\frac{dR}{d\varphi} \right) \frac{1}{\alpha(2\mu_0 H_{\text{FMR}} + \mu_0 M_{\text{eff}})} \tau_{\parallel} \quad (1)$$

$$V_{\text{mix},A} = -\frac{I_{\text{rf}}}{2} \left(\frac{dR}{d\varphi} \right) \frac{\sqrt{1 + M_{\text{eff}}/H_{\text{FMR}}}}{\alpha(2\mu_0 H_{\text{FMR}} + \mu_0 M_{\text{eff}})} \tau_{\perp} \quad (2)$$

where I_{rf} is the microwave current, R is the device resistance as a function of in-plane magnetic field angle φ due to the AMR of Py, α is the Gilbert damping coefficient, and M_{eff} is the effective magnetization. The AMR of Py is determined by measuring the device resistance as a function of magnetic field angle with a field magnitude of 0.1 T. We calibrate the microwave current I_{rf} by measuring the microwave current induced device resistance change due to Joule heating^{36,37} (Supplementary Note 6). The in-plane and out-of-plane torques can be expressed as the angular dependence of the torque components with different spin polarization directions,

$$\tau_{\parallel} = \tau_{x,AD} \sin(\varphi) + \tau_{y,AD} \cos(\varphi) + \tau_{z,FL} \quad (3)$$

$$\tau_{\perp} = \tau_{x,FL} \sin(\varphi) + \tau_{y,FL} \cos(\varphi) + \tau_{z,AD} \quad (4)$$

The strength of the torque components can then be determined from equations (1-4) with the calibrated I_{rf} values, from which we noticed that the primary contribution to $\tau_{y,FL}$ is the current-induced Oersted field. The spin torque ratios can be expressed as,

$$\theta_x = \frac{\tau_{x,AD}}{\tau_{y,FL}} \frac{e\mu_0 M_s t_{Py} t_{MGN}}{\hbar} \sqrt{1 + M_{eff}/H_{FMR}} \quad (5)$$

$$\theta_y = \frac{\tau_{y,AD}}{\tau_{y,FL}} \frac{e\mu_0 M_s t_{Py} t_{MGN}}{\hbar} \sqrt{1 + M_{eff}/H_{FMR}} \quad (6)$$

$$\theta_z = \frac{\tau_{z,AD}}{\tau_{y,FL}} \frac{e\mu_0 M_s t_{Py} t_{MGN}}{\hbar} \quad (7)$$

where M_s and t_{Py} are the saturation magnetization and the thickness of Py; t_{MGN} is the thickness of MGN. \hbar is the reduced Planck's constant and e is the electron charge. The saturation magnetization of Py was measured with SQUID magnetometry, and is indistinguishable from the effective magnetization determined by ST-FMR.

Electrical transport measurements of Mn₃GaN

Electrical transport measurements of Mn₃GaN films were performed directly on as-grown films wire-bonded in a four-corner van der Pauw geometry. Both sheet resistance and Hall resistance were measured as a function of temperature and magnetic induction in a Quantum Design Physical Property Measurement System. Film resistivity was computed by solving the van der Pauw equation in conjunction with film thickness as measured with x-ray reflectivity, while Hall resistance was calculated by summing two orthogonal Hall configurations. The longitudinal resistivity and the Hall resistance of Mn₃GaN films vs. temperature are reported in the Supplementary Figure 4.

Temperature dependence of neutron diffraction

Single crystal neutron diffraction measurements were performed on the WISH time-of-flight diffractometer³⁸ at ISIS, the UK neutron and muon source. A stack of eight, approximately 250 nm thick (001) Mn₃GaN film samples with lateral dimensions 10 x 8 mm, were co-aligned and oriented for the measurement of nuclear and magnetic diffraction intensities in the (HK0) reciprocal lattice plane. The sample was first mounted within a ⁴He cryostat, and diffraction patterns were collected from a base temperature of 1.5 K up to 300 K, in 25 K steps. The sample was transferred to a medium-range furnace, and diffraction patterns were then collected at 320, 340, 360 and 390 K.

Temperature dependence of X-ray diffraction

The x-ray diffraction data were acquired at beamline 6-ID-B at the Advanced Photon Source with 12 keV incident x-ray energy. The sample temperature was controlled employing an ARS high temperature cryostat. Data were collected with 5 K steps; and at each temperature the sample position was realigned with respect to the base-temperature reciprocal space matrix. The sample was mounted on a standard PSI Huber diffractometer. The representative temperature dependence of x-ray diffraction spectra around the LSAT (003) reflection can be found in Supplementary Figure 2.

Theoretical calculations

The electronic band structure of Mn₃GaN was calculated by using first-principles density functional theory (DFT) with Quantum ESPRESSO³⁹ and fully relativistic ultrasoft pseudopotentials⁴⁰. The exchange and correlation effects were treated within the generalized gradient approximation (GGA)⁴¹. The plane-wave cut-off energy of 57 Ry and a 16 × 16 × 16 k -point mesh in the irreducible Brillouin zone were used

in the calculations. Spin-orbit coupling and noncollinear Γ^{5g} antiferromagnetism were included in all electronic structure calculations. We note that even though the spin-orbit coupling in Mn_3GaN is relatively small, it still plays an important role to couple the spin and the lattice, which lifts the spin rotation symmetry and allows the existence of the non-vanishing spin Hall conductivity (Supplementary Note 10). The calculated band structures for Mn_3GaN in antiferromagnetic and paramagnetic phases are shown in Supplementary Figure 9.

The spin Hall effect is given by⁴²

$$\sigma_{ij}^k = \frac{e^2}{\hbar} \int \frac{d^3\vec{k}}{(2\pi)^3} \sum_n f_{n\vec{k}} \Omega_{n,ij}^k(\vec{k}) \quad (8)$$

$$\Omega_{n,ij}^k(\vec{k}) = -2\text{Im} \sum_{n \neq n'} \frac{\langle n\vec{k} | J_i^k | n'\vec{k} \rangle \langle n'\vec{k} | v_j | n\vec{k} \rangle}{(E_{n\vec{k}} - E_{n'\vec{k}})^2} \quad (9)$$

where $f_{n\vec{k}}$ is the Fermi-Dirac distribution for the n th band, $J_i^k = \frac{1}{2}\{v_i, s_k\}$ is the spin current operator with spin operator s_k , $v_j = \frac{1}{\hbar} \frac{\partial H}{\partial k_j}$ is the velocity operator, and $i, j, k = x, y, z$. $\Omega_{n,ij}^k(\vec{k})$ is referred to as the spin Berry curvature in analogy to the ordinary Berry curvature. In order to calculate the spin Hall conductivities, we construct the tight-binding Hamiltonians using PAOFLOW code⁴³ based on the projection of the pseudo-atomic orbitals (PAO)^{44,45} from the non-self-consistent calculations with a $16 \times 16 \times 16$ k -point mesh. The spin Hall conductivities were calculated using the tight-binding Hamiltonians with a $48 \times 48 \times 48$ k -point mesh by the adaptive broadening method to get the converged values.

Synchrotron spectroscopy and microscopy

X-ray magnetic circular dichroism (XMCD) and X-ray magnetic linear dichroism (XMLD) spectroscopy were measured at beamline 4.0.2, and x-ray microscopy at beamline 11.0.1.1 (PEEM-3) at the Advanced Light Source (ALS). In spectroscopy, total-electron-yield mode was employed by monitoring the sample drain current, and a grazing incidence angle of 30° to the sample surface along the $[110]$ direction to probe the magnetic state. Hysteresis curves were obtained by monitoring the Fe and Mn L_3 -edge XMCD as function of applied field. The obtained dichroism energies giving information on the magnetic nature of the Mn_3GaN were then used to image the domain texture by x-ray photoemission electron microscopy (XPEEM), also taken with x-rays at a 30° grazing incidence along the $[110]$ direction. Images taken at the maximum dichroism energies as a function of polarization were normalized by pre-edge energy images in order to minimize any topographic and work function contrast while emphasizing the magnetic contrast of the Mn_3GaN films.

Data availability

The data that support the findings of this study are available from the corresponding author on reasonable request.

References

1. Ando, K. *et al.* Electric manipulation of spin relaxation using the spin hall effect. *Phys. Rev. Lett.* **101**, 036601 (2008).
2. Gambardella, P. & Miron, I. M. Current-induced spin-orbit torques. *Philos. Trans. R. Soc. A Math. Phys. Eng. Sci.* **369**, 3175–3197 (2011).
3. Brataas, A., Kent, A. D. & Ohno, H. Current-induced torques in magnetic materials. *Nat. Mater.* **11**, 372–381 (2012).
4. Liu, L. *et al.* Spin-torque switching with the giant spin hall effect of tantalum. *Science* **336**, 555–558 (2012).
5. Kim, J. *et al.* Layer thickness dependence of the current-induced effective field vector in Ta|CoFeB|MgO. *Nat. Mater.* **12**, 240–245 (2013).
6. Emori, S., Bauer, U., Ahn, S.-M., Martinez, E. & Beach, G. S. D. Current-driven dynamics of chiral ferromagnetic domain walls. *Nat. Mater.* **12**, 611–616 (2013).
7. Fan, X. *et al.* Quantifying interface and bulk contributions to spin-orbit torque in magnetic bilayers. *Nat. Commun.* **5**, 3042 (2014).
8. Mellnik, A. R. *et al.* Spin-transfer torque generated by a topological insulator. *Nature* **511**, 449–451 (2014).
9. Dyakonov, M. I. & Perel, V. I. Current-induced spin orientation of electrons in semiconductors. *Phys. Lett. A* **35**, 459–460 (1971).
10. Sinova, J., Valenzuela, S. O., Wunderlich, J., Back, C. H. & Jungwirth, T. Spin Hall effects. *Rev. Mod. Phys.* **87**, 1213–1260 (2015).
11. Fukami, S., Anekawa, T., Zhang, C. & Ohno, H. A spin-orbit torque switching scheme with collinear magnetic easy axis and current configuration. *Nat. Nanotechnol.* **11**, 621–625 (2016).
12. Amin, V. P. & Stiles, M. D. Spin transport at interfaces with spin-orbit coupling: Phenomenology. *Phys. Rev. B* **94**, 104420 (2016).
13. Baek, S. H. C. *et al.* Spin currents and spin-orbit torques in ferromagnetic trilayers. *Nat. Mater.* **17**, 509–513 (2018).
14. Humphries, A. M. *et al.* Observation of spin-orbit effects with spin rotation symmetry. *Nat. Commun.* **8**, 911 (2017).
15. MacNeill, D. *et al.* Control of spin-orbit torques through crystal symmetry in WTe₂/ferromagnet bilayers. *Nat. Phys.* **13**, 300–305 (2016).
16. Fang, D. *et al.* Spin-orbit-driven ferromagnetic resonance. *Nat. Nanotechnol.* **6**, 413–417 (2011).
17. Kurebayashi, H. *et al.* An antidamping spin-orbit torque originating from the Berry curvature. *Nat. Nanotechnol.* **9**, 211–217 (2014).
18. Ciccarelli, C. *et al.* Room-temperature spin-orbit torque in NiMnSb. *Nat. Phys.* **12**, 855–860 (2016).
19. Zhang, W. *et al.* Spin hall effects in metallic antiferromagnets. *Phys. Rev. Lett.* **113**, 196602 (2014).
20. Zhang, W. *et al.* Giant facet-dependent spin-orbit torque and spin Hall conductivity in the

- triangular antiferromagnet IrMn₃. *Sci. Adv.* **2**, e1600759 (2016).
21. Fukami, S., Zhang, C., DuttaGupta, S., Kurenkov, A. & Ohno, H. Magnetization switching by spin-orbit torque in an antiferromagnet-ferromagnet bilayer system. *Nat. Mater.* **15**, 535–541 (2016).
 22. Kimata, M. *et al.* Magnetic and magnetic inverse spin Hall effects in a non-collinear antiferromagnet. *Nature* **565**, 627–630 (2019).
 23. Bertaut, E. F., Fruchart, D., Bouchaud, J. P. & Fruchart, R. Diffraction neutronique de Mn₃GaN. *Solid State Commun.* **6**, 251–256 (1968).
 24. Shi, K. *et al.* Baromagnetic effect in antiperovskite Mn₃Ga_{0.95}N_{0.94} by neutron powder diffraction analysis. *Adv. Mater.* **28**, 3761–3767 (2016).
 25. Matsunami, D., Fujita, A., Takenaka, K. & Kano, M. Giant barocaloric effect enhanced by the frustration of the antiferromagnetic phase in Mn₃GaN. *Nat. Mater.* **14**, 73–78 (2015).
 26. Liu, L., Moriyama, T., Ralph, D. C. & Buhrman, R. A. Spin-torque ferromagnetic resonance induced by the spin Hall effect. *Phys. Rev. Lett.* **106**, 036601 (2011).
 27. Garello, K. *et al.* Symmetry and magnitude of spin-orbit torques in ferromagnetic heterostructures. *Nat. Nanotechnol.* **8**, 587–593 (2013).
 28. Železný, J., Zhang, Y., Felser, C. & Yan, B. Spin-Polarized Current in Noncollinear Antiferromagnets. *Phys. Rev. Lett.* **119**, 187204 (2017).
 29. Takenaka, K. & Takagi, H. Giant negative thermal expansion in Ge-doped anti-perovskite manganese nitrides. *Appl. Phys. Lett.* **87**, 261902 (2005).
 30. Ou, Y., Ralph, D. C. & Buhrman, R. A. Strong enhancement of the spin Hall effect by spin fluctuations near the Curie point of FePt_{1-x} alloys. *Phys. Rev. Lett.* **120**, 097203 (2018).
 31. MacDonald, A. H. & Tsoi, M. Antiferromagnetic metal spintronics. *Philos. Trans. R. Soc. A Math. Phys. Eng. Sci.* **369**, 3098–3114 (2011).
 32. Jungwirth, T., Marti, X., Wadley, P. & Wunderlich, J. Antiferromagnetic spintronics. *Nat. Nanotechnol.* **11**, 231–241 (2016).
 33. Wadley, P. *et al.* Electrical switching of an antiferromagnet. *Science* **351**, 587–590 (2016).
 34. Železný, J., Wadley, P., Olejník, K., Hoffmann, A. & Ohno, H. Spin transport and spin torque in antiferromagnetic devices. *Nat. Phys.* **14**, 220–228 (2018).
 35. Baltz, V. *et al.* Antiferromagnetic spintronics. *Rev. Mod. Phys.* **90**, 015005 (2018).
 36. Tshitoyan, V. *et al.* Electrical manipulation of ferromagnetic NiFe by antiferromagnetic IrMn. *Phys. Rev. B* **92**, 214406 (2015).
 37. Zhang, W. *et al.* All-electrical manipulation of magnetization dynamics in a ferromagnet by antiferromagnets with anisotropic spin Hall effects. *Phys. Rev. B* **92**, 144405 (2015).
 38. Chapon, L. C. *et al.* Wish: The new powder and single crystal magnetic diffractometer on the second target station. *Neutron News* **22**, 22–25 (2011).
 39. Giannozzi, P. *et al.* QUANTUM ESPRESSO: A modular and open-source software project for quantum simulations of materials. *J. Phys. Condens. Matter* **21**, 395502 (2009).

- 40. Vanderbilt, D. Soft self-consistent pseudopotentials in a generalized eigenvalue formalism. *Phys. Rev. B* **41**, 7892–7895 (1990).
- 41. Perdew, J. P., Burke, K. & Ernzerhof, M. Generalized gradient approximation made simple. *Phys. Rev. Lett.* **77**, 3865–3868 (1996).
- 42. Gradhand, M. *et al.* First-principle calculations of the Berry curvature of Bloch states for charge and spin transport of electrons. *Journal of Physics Condensed Matter* **24**, 213202 (2012).
- 43. Buongiorno Nardelli, M. *et al.* PAOFLOW: A utility to construct and operate on ab initio Hamiltonians from the projections of electronic wavefunctions on atomic orbital bases, including characterization of topological materials. *Comput. Mater. Sci.* **143**, 462–472 (2018).
- 44. Agapito, L. A., Ferretti, A., Calzolari, A., Curtarolo, S. & Buongiorno Nardelli, M. Effective and accurate representation of extended Bloch states on finite Hilbert spaces. *Phys. Rev. B* **88**, 165127 (2013).
- 45. Agapito, L. A., Ismail-Beigi, S., Curtarolo, S., Fornari, M. & Nardelli, M. B. Accurate tight-binding Hamiltonian matrices from ab initio calculations: Minimal basis sets. *Phys. Rev. B* **93**, 035104 (2016).

Acknowledgments

This work was supported by the National Science Foundation (NSF) under DMREF Grant DMR-1629270, the University of Wisconsin Materials Research Science and Engineering Center (DMR-1720415), the Army Research Office through Grant W911NF-17-1-0462 and AFOSR FA9550-15-1-0334. Transport and magnetization measurement at the University of Wisconsin-Madison was supported by the US Department of Energy (DOE), Office of Science, Office of Basic Energy Sciences under Award DE-FG02-06ER46327. Theoretical research at University of Nebraska-Lincoln (UNL) was partly supported by the NSF Materials Research Science and Engineering Center (MRSEC) program under Grant DMR-1420645. Computations were performed at the UNL's Holland Computing Center. Work at Cornell was supported by the NSF (DMR-1708499), and was performed in part at the Cornell NanoScale Facility, an NNCI member supported by NSF Grant NNCI-1542081 and also in part in the shared facilities of the Cornell Center for Materials Research which are supported by the NSF MRSEC program (DMR-1719875). This research used resources of the Advanced Photon Source, a U.S. DOE Office of Science User Facility operated for the DOE Office of Science by Argonne National Laboratory under Contract No. DE-AC02-06CH11357. This research used resources of the Advanced Light Source, which is a DOE Office of Science User Facility under contract no. DE-AC02-05CH11231.

Author Contributions

T.N. and C.B.E. conceived the research. C.B.E., M.S.R., E.Y.T., D.C.R., P.G.R., T.T. and S.Y.C. supervised the experiments. T.N., C.X.Q., and L.G. performed the sample growth and surface/structural characterizations. T.N. performed the device fabrication. T.N., and J.G. performed ST-FMR measurements and analysis. N.C. and J.I. performed magnetic and electrical transport characterizations. G.G. and D.F.S. performed the theoretical calculations. K.S. and S.Y.C. carried out the high-resolution TEM experiments. R.D.J., P.M. and P.G.R. conceived and performed the neutron diffraction experiment. P.R., J.W.K. and Y.S.C. carried out the synchrotron diffraction measurements. R.V.C. and I.H. performed synchrotron spectroscopy measurements, and R.V.C. performed and analyzed synchrotron microscopy measurements. T.N., J.I., D.F.S., D.C.R. and C.B.E. wrote the manuscript. All authors discussed the results and commented on the manuscript. C.B.E. directed the research.

Competition interests

T.N. and C.B.E. have filed a patent on the technology in this paper. The remaining authors declare no competing interests.

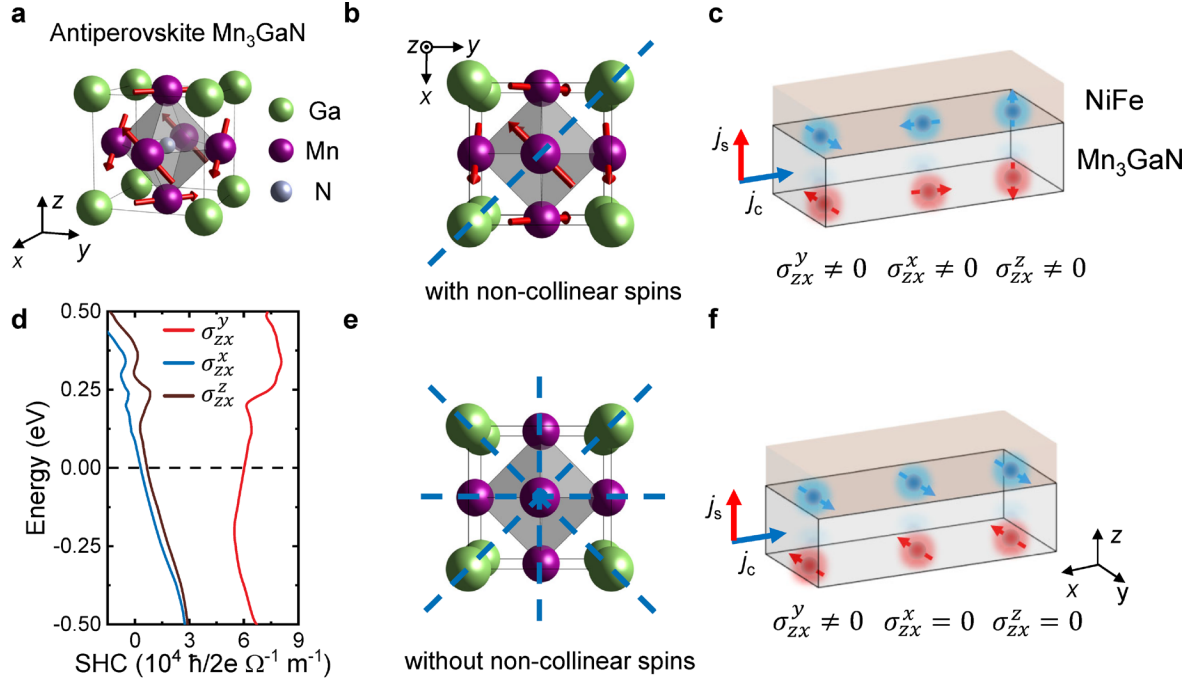


Fig. 1 | The concept of the unconventional spin-Hall effect in Mn_3GaN . **a**, The crystallographic unit cell of antiperovskite Mn_3GaN with the antiferromagnetic Γ^{5g} spin structure where Mn spins (arrows) form a Kagome-type lattice in the (111) plane. **x**, **y**, and **z** correspond to the cubic [100], [010], and [001] axes, respectively. **b**, Spin structure of Mn_3GaN projected onto the (001) plane. The blue dashed line corresponds to the (110) mirror plane. **c**, Schematic illustrations of the Py/ Mn_3GaN bilayer and the allowed spin-Hall spin polarization in the low-symmetry state (**a**). This indicates non-zero spin-Hall conductivities σ_{zx}^y , σ_{zx}^x and σ_{zx}^z , which correspond to spin polarizations along **y**, **x** and **z** direction, respectively (with the charge current along **x** and spin flow along **z**). **d**, Calculated spin-Hall conductivities σ_{zx}^y , σ_{zx}^x and σ_{zx}^z for Mn_3GaN in the antiferromagnetic phase as a function of Fermi energy. **e**, Crystal structure of Mn_3GaN without non-collinear spin structure (i.e. above the antiferromagnetic transition temperature T_N) in the (001) plane, which gives rise to a high-symmetry state. **f**, Allowed spin polarization in the high-symmetry state, where only the conventional spin-Hall conductivity σ_{zx}^y is non-zero.

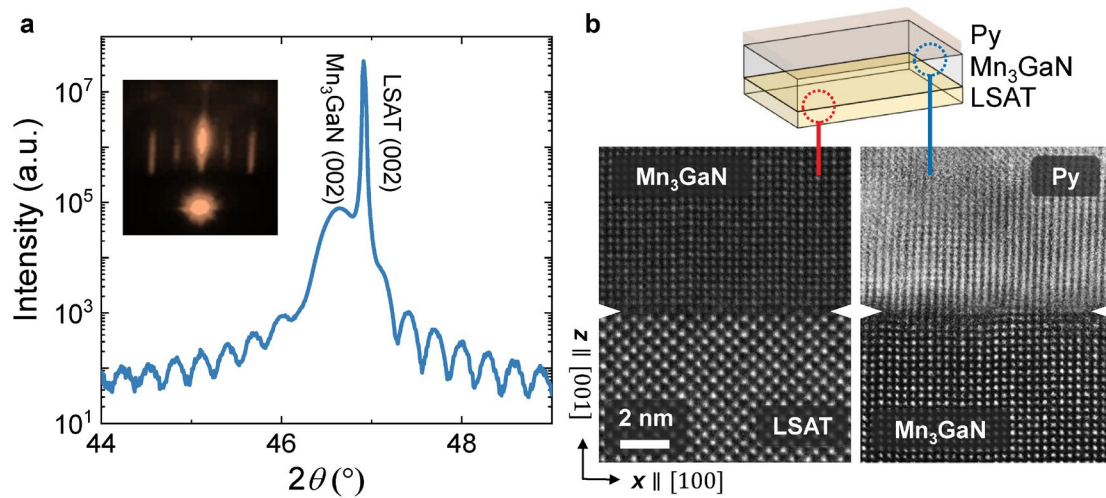


Fig. 2 | Structural characterization of the Py/Mn₃GaN/LSAT. **a**, 2θ - ω x-ray scan of the heterostructure of 10 nm Py/30 nm Mn₃GaN on LSAT (001) substrate showing single-phase Mn₃GaN with thickness oscillations indicating a smooth surface and sharp interface with the substrate. Inset shows reflection high-energy electron diffraction (RHEED) pattern of the specular diffraction spot for the Mn₃GaN surface. **b**, Scanning transmission electron microscope image of Py/Mn₃GaN heterostructure on (001) LSAT substrate with the top Py/Mn₃GaN interface (left), and the bottom Mn₃GaN/LSAT interface (right).

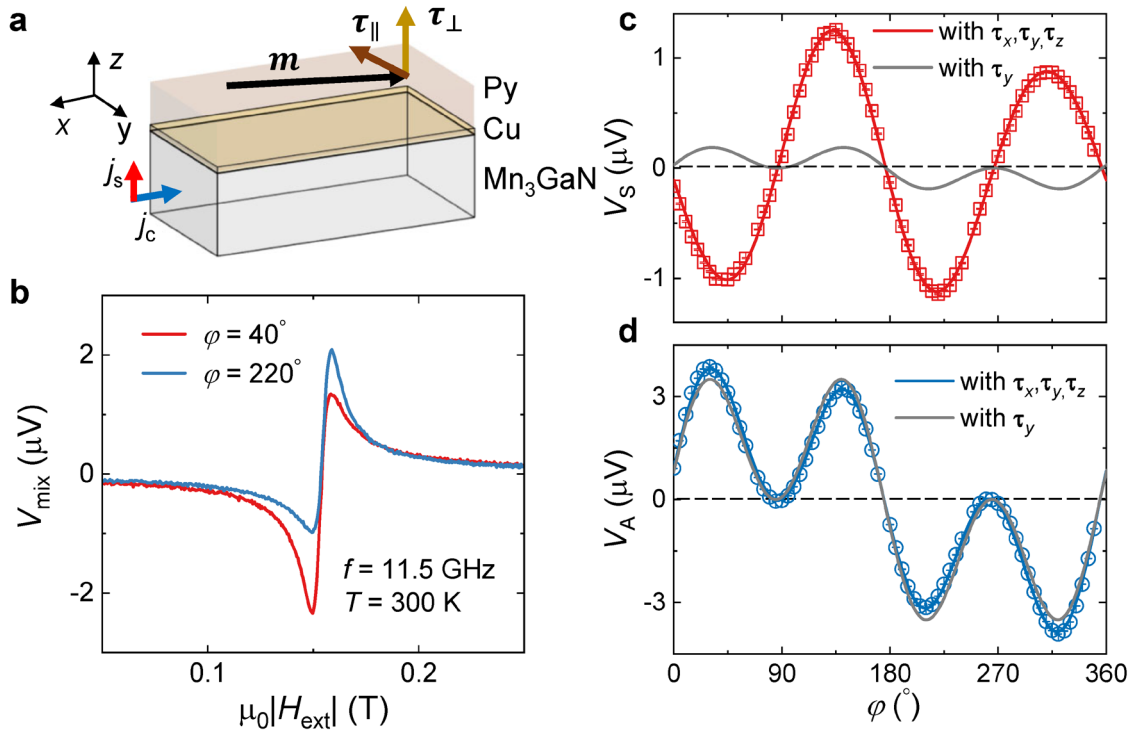


Fig. 3 | ST-FMR measurements. **a**, Schematic of the ST-FMR geometry for the Py/Cu/Mn₃GaN structures. τ_{\parallel} and τ_{\perp} denote the in-plane and out-of-plane torque components, which consist of different torque terms. **b**, ST-FMR spectra for the 10 nm Py/2nm Cu/20 nm Mn₃GaN device at 300 K (antiferromagnetic phase) with the Py magnetization oriented at 40° and 220° relative to the current axis. **c**, **d**, Symmetric (**c**) and antisymmetric (**d**) ST-FMR components for the 10 nm Py/2nm Cu/20 nm Mn₃GaN device as a function of the in-plane magnetic field angle at 300 K. The microwave current is applied along the [100] direction (x axis). The applied microwave frequency and power are 11.5 GHz and 15 dBm, respectively. The error bars indicate fitting uncertainties.

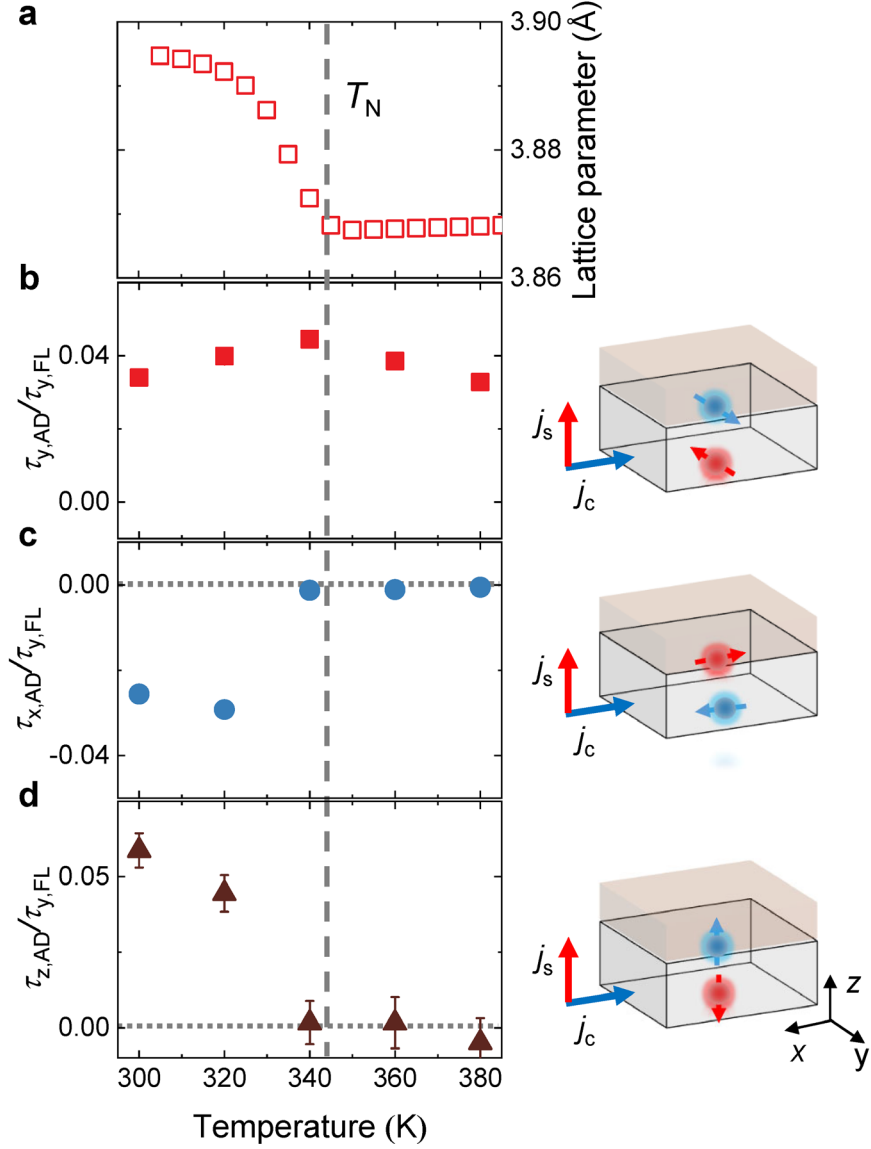


Fig. 4 | Temperature dependence of spin-orbit torques. **a**, Out-of-plane lattice parameter of a 30 nm $\text{Mn}_3\text{GaN}/\text{LSAT}$ sample as a function of temperature; the lattice parameters anomaly indicates the Mn_3GaN Néel temperature T_N of ~ 345 K. **b-d**, The torque ratios $\tau_{y,AD}/\tau_{y,FL}$, $\tau_{x,AD}/\tau_{y,FL}$ and $\tau_{z,AD}/\tau_{y,FL}$ as a function of the temperature. The schematics on the right panel show the geometry of the spin-Hall effect with different spin polarizations. The error bars indicate fitting uncertainties. Some of them are smaller than the size of the symbols.